ADVANCES IN ATMOSPHERIC SCIENCES, VOL. 33, NOVEMBER 2016, 1259–1270

Mesoscale Modeling Study of Severe Convection over Complex Terrain

Ying ZHANG[1], Zhiyong MENG[2], Peijun ZHU[1], Tao SU[1], and Guoqing ZHAI*[1]

[1]*Department of Atmospheric Sciences, School of Earth Sciences, Zhejiang University, Hangzhou* 310007*, China*
[2]*Department of Atmospheric and Oceanic Sciences, School of Physics, Peking University, Beijing* 100080*, China*

(Received 12 October 2015; revised 17 July 2016; accepted 8 August 2016)

ABSTRACT

Short squall lines that occurred over Lishui, southwestern Zhejiang Province, China, on 5 July 2012, were investigated using the WRF model based on $1^\circ \times 1^\circ$ gridded NCEP Final Operational Global Analysis data. The results from the numerical simulations were particularly satisfactory in the simulated radar echo, which realistically reproduced the generation and development of the convective cells during the period of severe convection. The initiation of this severe convective case was mainly associated with the uplift effect of mesoscale mountains, topographic convergence, sufficient water vapor, and enhanced low-level southeasterly wind from the East China Sea. An obvious wind velocity gradient occurred between the Donggong Mountains and the southeast coastline, which easily enabled wind convergence on the windward slope of the Donggong Mountains; both strong mid–low-level southwesterly wind and low-level southeasterly wind enhanced vertical shear over the mountains to form instability; and a vertical coupling relation between the divergence on the upper-left side of the Donggong Mountains and the convergence on the lower-left side caused the convection to develop rapidly. The convergence centers of surface streams occurred over the mountain terrain and updrafts easily broke through the lifting condensation level (LCL) because of the strong wind convergence and topographic lift, which led to water vapor condensation above the LCL and the generation of the initial convective cloud. The centers of surface convergence continually created new convective cells that moved with the southwest wind and combined along the Donggong Mountains, eventually forming a short squall line that caused severe convective weather.

Key words: mesoscale mountains, mountain squall line, severe convective weather

Citation: Zhang, Y., Z. Y. Meng, P. J. Zhu, T. Su, and G. Q. Zhai, 2016: Mesoscale modeling study of severe convection over complex terrain. *Adv. Atmos. Sci.*, **33**(11), 1259–1270, doi: 10.1007/s00376-016-5221-0.

1. Introduction

The conditions that trigger severe convection over mountainous terrain are highly complex, particularly over mesoscale terrain. In recent decades, the trigger and enhancement mechanisms of orographic precipitation have been identified as thermodynamic factors as well as dynamical and orographic factors such as shape and size (Smith, 1979; Roe, 2005). The effect of mountainous topography plays a very important role for weather in China. Tao (1980) reported topography to have a considerable influence on the triggering and growth of heavy rain in China. Chen et al. (1995) analyzed the impact of mountainous terrain on heavy rain under various natural conditions and reported that the influence of heavy rain to vary widely among different terrain types with the same geographical background. Topography-forced lifting and topographic convergence are important mechanisms for the triggering and growth of heavy rain in mountainous regions, whereas topographic divergence and downdraft areas correspond to low-frequency regions. Many researchers have used numerical models to study the impact of topography on rainfall in China, in which the effect of the terrain on precipitation under particular weather conditions has been considered (Yue et al., 2005; Li et al., 2007).

The thermally driven local wind system in mountainous areas also plays a very important role in the triggering of convection (Raymond and Wilkening, 1980; Toth and Johnson, 1985). Large amounts of solar radiation contribute to the development of slope and valley winds, and high evapotranspiration leads to an increase of moisture in the PBL. Thermally driven circulation systems form a convergence zone along mountain crests, which often results in severe convection. In dynamic terms, Tao (1980) considered the windward slope of the terrain to have a blocking effect that forces the flow to climb or split around the terrain, reporting that mountain terrain can also trigger a severe convection system to cause the release of instability energy.

The cyclonic convergence caused by the effect of the terrain is often the basic environment of heavy rain events (Rudari et al., 2004). Therefore, cumulus clouds accompanied by sufficient dynamic lifting and moisture convergence are prone to generating local rainstorms. Early studies determined that in areas with no large-scale weather, low-level

* Corresponding author: Guoqing ZHAI
Email: zhaigq@zju.edu.cn

convergence zones are the initial locations of convection (Byers and Braham, 1949; Purdom and Marcus, 1982; Wilson and Schreiber, 1986). However, these low-level convergence zones are generally ignored because of the complexity of the topography and low density of automatic weather stations. A possible explanation for the location and timing of convection initiation (CI) is that boundary layer convergence zones often form and force new deep and moist convection (Weckwerth et al., 2014).

Mesoscale mountains, such as the small hills of South China and other regions, have an important impact on the arriving airflow, as well as on severe convection at the local level. Although the interaction between the terrain and atmosphere is highly complex, researchers consider the effect of terrain in precipitation studies because it is highly important in the generation and development of local heavy rain. Therefore, many scholars have conducted numerical simulation work in studies of topography-related precipitation (Meißner et al., 2007; Barthlott and Kirshbaum, 2013).

Local severe convection in complex terrain regions often indicates that the terrain plays a role in the triggering of severe convection. However, rainfall is a highly complicated physical process. Orographic precipitation is not only limited to the local vertical motion caused by orographic lift, but also to the rainfall caused by changes in the weather system owing to the orographic dynamical effect. However, if the atmospheric environment approaches instability, other disturbances or trigger mechanisms are likely, which makes it difficult to separate the topographic effects. Therefore, verification of topographic lift as the only trigger of orographic precipitation is difficult.

Researchers worldwide have considered terrain effects to often be the main triggers of topographic precipitation. Zhejiang Province, a coastal area in Southeast China, has unique geographic and geomorphic characteristics, including the Donggong Mountains (Fig. 1b). The role of coastal mesoscale terrain in severe convection is unknown, particularly for the initiation of a short mountain squall lines, and the mesoscale features of the convection mechanism. Therefore, in this study, we conducted a WRF model simulation to examine these factors. Specifically, we selected a typical short squall line case that occurred over Zhejiang's southeastern mountains, which we introduce briefly in section 2 along with the large-scale synoptic conditions. A description of the experimental design and large-scale data is provided in section 3. Comparisons between the model-produced and observed thermal conditions, surface wind field and radar reflectivity, rainfall rates, and synoptic conditions, are presented in section 4. Section 5 analyzes the simulated surface stream and divergence, CI, and instability mechanism results. A discussion on the effect of the sea breeze is presented in section 6, followed by conclusions in section 7.

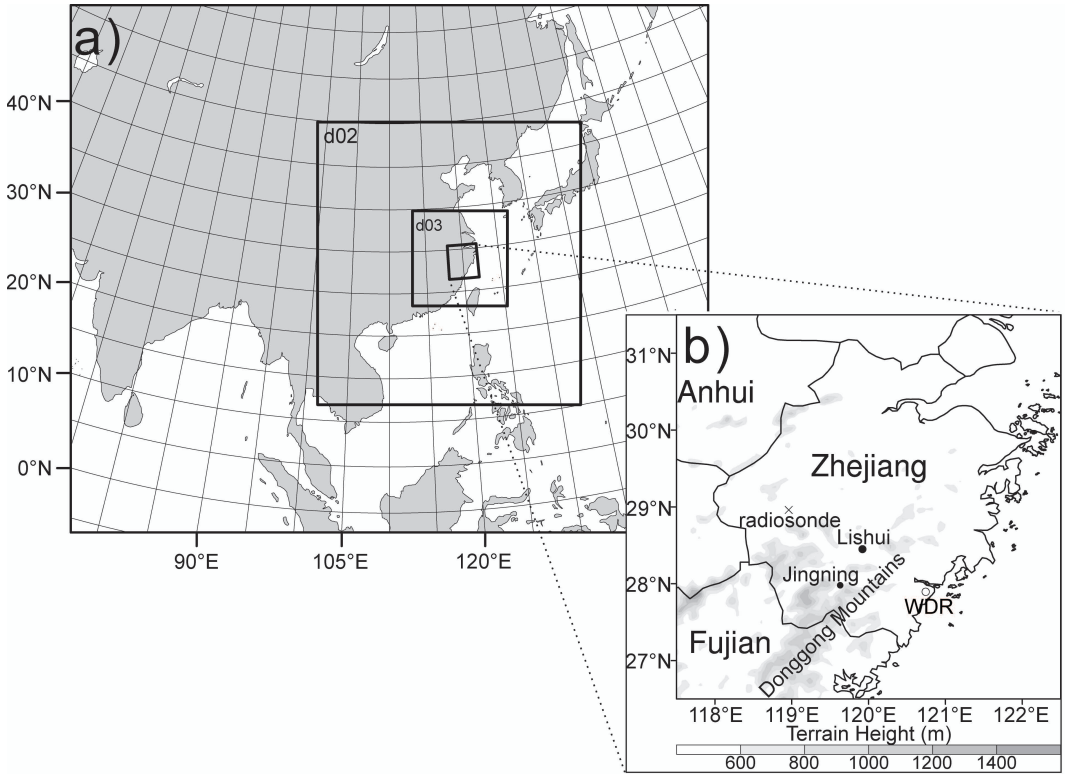

Fig. 1. (a) The three WRF domains used in this study. The map size is the outer domain; the d02 and d03 boxes indicate the second and third domains, respectively. The inset shows a map of Zhejiang Province. (b) Terrain-contoured base map of Zhejiang Province and its surrounding areas. The Donggong Mountains are located at the junction of Zhejiang and Fujian provinces. The black dots show the locations of Lishui and Jingning weather stations; the open circle represents the Wenzhou Doppler Radar (WDR); and the cross marks Quxian radiosonde station.

2. Case description

The low mountainous terrain of the southeastern Zhejiang Province and Fujian Province border region (Fig. 1b) often produces mesoscale convective cells that can cause local severe weather. To examine the occurrence and development of severe convective weather over coastal mesoscale terrain, we selected a short squall line that occurred on 5 July 2012 over the southern mountains in Zhejiang as a case study. This short squall line mainly moved along the southwest–northeast direction of the Donggong Mountains, and ultimately produced severe weather on the eastern side of the mountains (see Fig. 2c).

Figure 2a shows that at 0000 UTC 5 July 2012 a shallow trough slowly traveled eastward in East China at 500 hPa. Zhejiang Province was under the northwest shoulder of the western Pacific subtropical high; the 588 dagpm isoline passed through the north of Zhejiang. A southwesterly airstream had been maintained in the Lishui area at 850 hPa, which transported a steady stream of water vapor. Southern Zhejiang was mainly in the warm sector, which caused instability in the atmospheric stratification to provide favorable large-scale background conditions for strong convective weather. According to the blackbody temperature (TBB) image (Fig. 2b), there was a mass of convective clouds in southern Zhejiang Province, and it is clear that the convective clouds of this process were isolated and localized (see the red box in Fig. 2b). Figure 2c demonstrates that the disastrous weather in the area indicated by the red box in Fig. 2b was short in duration (1000–1200 UTC) and low in range. The accumulated rainfall during the two hours from 1000 to 1200 UTC, as recorded by multiple observation stations in the Lishui area, was more than 25 mm, indicating a short-term rainstorm; the maximum accumulated precipitation was 74 mm. The distribution of this 2-h accumulated precipitation was mainly in the region of the radar echo at 1100 UTC and to its east (Fig. 2c). Moreover, a hailstorm occurred for several minutes at approximately 1040 UTC, and multiple locations in Lishui experienced thunderstorms and gales during the period of severe convection, with a maximum surface wind speed of 24.5 m s^{-1}. Disastrous weather occurred mainly near Jingning County, in the northeastern Donggong Mountains, which caused considerable economic losses in the region.

To reveal the occurrence mechanism of this severe convection process over complex terrain, dense surface observation data, Wenzhou Doppler radar (WDR) data and numerical simulation data were used to explore the severe convection triggers in Lishui.

3. WRF simulations

Version 3.5.1 of the WRF mesoscale numerical model was used in this study. The three nested domains (D1, D2, D3; Fig. 1a) were centered on (28°N, 118°E), with two-way nesting schemes adopted. The horizontal grid resolutions were 36, 12 and 4 km, with 236 × 195, 292 × 313 and

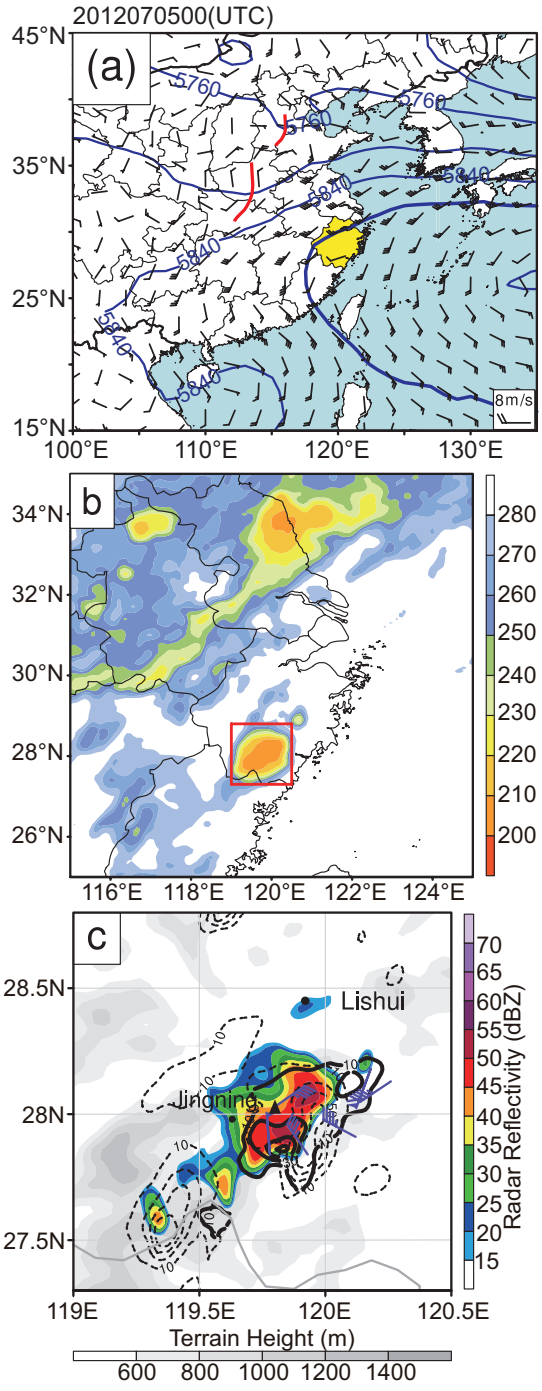

Fig. 2. (a) 500 hPa geopotential height field (blue lines, units: gpm), the bold blue line is 5880 geopotential meters, the thick red lines are trough lines, and 850 hPa wind field at 0000 UTC 5 July 2012. (b) TBB at 1200 UTC 5 July 2012. (c) Two-hour accumulated precipitation (solid black contours for observed and dotted black contours for simulated results; units: mm), in the red box in (b). Wind barbs represent observed surface station wind speed ⩾17.2 m s^{-1}, and the black triangle represents the location of the automatic station that reported hail. The color legend on the right indicates the composite reflectivity (units: dBZ) from the WDR (marked by the open circle in Fig. 1b) at 1100 UTC. The color legend at the bottom indicates the terrain height (units: m).

316 × 316 grid points for D1, D2 and D3, respectively. In order to obtain a finer simulated result in the vertical direction, we increased the density of vertical layers to 57 levels, ranging from the ground to 50 hPa. The model physical parameterizations included WSM6 (Hong and Lim, 2006), the Mellor–Yamada–Janjic turbulent kinetic energy PBL scheme (Janjić, 1994), the Kain–Fritsch (new Eta) cumulus scheme (for D1 and D2 only; Kain and Fritsch, 1993), and the Noah land surface scheme (Chen and Dudhia, 2001). NCEP Final Operational Global Analysis data, on 1° × 1° grids, prepared operationally every six hours, were used as the initial fields and lateral boundary conditions. The integration time period was 24 hours, from 0600 UTC 5 July to 0600 UTC 6 July 2012.

4. WRF–observation comparisons

To evaluate the performance of the WRF simulation, we compared the simulation results with observations. Specifically, we chose the sounding data from the nearest rawinsonde station (at Quxian), which is located approximately 150 km west of the convection occurrence at 1200 UTC 5 July 2012 (Fig. 1b), in order to compare with the large-scale WRF simulations. In Fig. 3, the observed sounding is shown in red and the simulation is shown in black. Except for the small difference in surface temperature and surface dew-point temperature between the simulation and observation (possibly associated with the complex underlying surface), the trends of the WRF temperature profile and dew-point temperature profile with height are almost consistent with the observation (see Fig. 3).

The analysis and comparison of observed and simulated ground wind field (Fig. 4) in the early stage clearly shows the ground wind field (data from automatic stations) convergence existed in the Donggong Mountain areas. This ground convergence airflow was composed of two flows. The first was from the northwest edge of the subtropical high known as southwest air flow, and the second was variable wind from the East China Sea affected by the friction of the coast that turned to the southeast wind near the coastline. The simulated radar echoes were compared with those observed by the Wenzhou Doppler Radar (WDR) (Fig. 5) to examine the occurrence of the convective weather under such background conditions.

Figure 5 compares the simulated and observed (WDR data) radar echoes during the period of severe convection. As can be seen, the WRF simulation largely reproduced the radar echoes. The simulated results in Figs. 5b, d and f agree with the results shown in Figs. 5a, c and e, during the occurrence and development of the severe convection. That is, the convective cells continually ascended over the mountains (Figs. 5a and c; Figs. 5b and d) and gradually formed a zonal echo along the mountains (Figs. 5e and f).

In analyzing the occurrence and development convection, we sorted the multiple cell echoes in the order of A, B, C and D from northeast to southwest (Fig. 5e). A small convective cell (A), which is shown in the radar reflectivity (dBZ) image

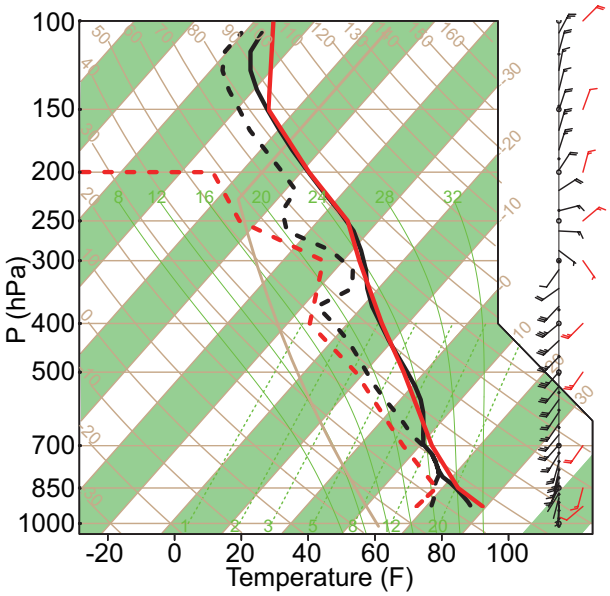

Fig. 3. Comparison of the Quxian rawinsonde station profile (red) and the WRF simulated profile (black) at 1200 UTC 5 July 2012. The dashed and solid lines indicate dew-point temperature and temperature, respectively.

in Fig. 5a, was also evident at a similar location in the simulation (Fig. 5b); however, the radar reflectivity in the simulations did not reach the trigger conditions. In this study, CI was defined as radar echoes exceeding 35 dBZ (May and Ballinger, 2007; Mecikalski et al., 2008; Anderson, 2010). At 0710 UTC, the radar reflectivity of the simulations of cells A and B (Fig. 5d) both exceeded 35 dBZ, which agreed with the echo intensity in the corresponding observation (Fig. 5c). Cells A, B, C and D showed development (Fig. 5e) and occurred in a linear arrangement that laid the foundation for the generation of the short squall line over the mountains. In contrast, after one hour's integration in the simulations, the corresponding cells appeared at similar locations. Cells B and C merged, and two echo centers were obvious. In addition, the strongest echo developed from cell C (Figs. 5g and h); therefore, we focused mainly on cell C in the present study. In summary, the experiment successfully simulated the radar echoes.

The precipitation during the convection process was concentrated mainly between 1000 and 1200 UTC (the solid black contours in Fig. 2c represent the two-hour observed accumulative precipitation, while the dotted black contours are for the same period but for the simulated precipitation). Comparison shows that the main precipitation area and precipitation intensity agreed with the observation in the northern mountains, while the simulated precipitation was larger in the Zhejiang Province and Fujian Province border region. In addition, compared with the synoptic conditions and other physical quantities (not shown), we detected agreement between the simulated results and observations, which contributed further to the verification of the WRF simulation of this case. Therefore, the results of the simulation were found to be appropriate for subsequent spatiotemporal analysis.

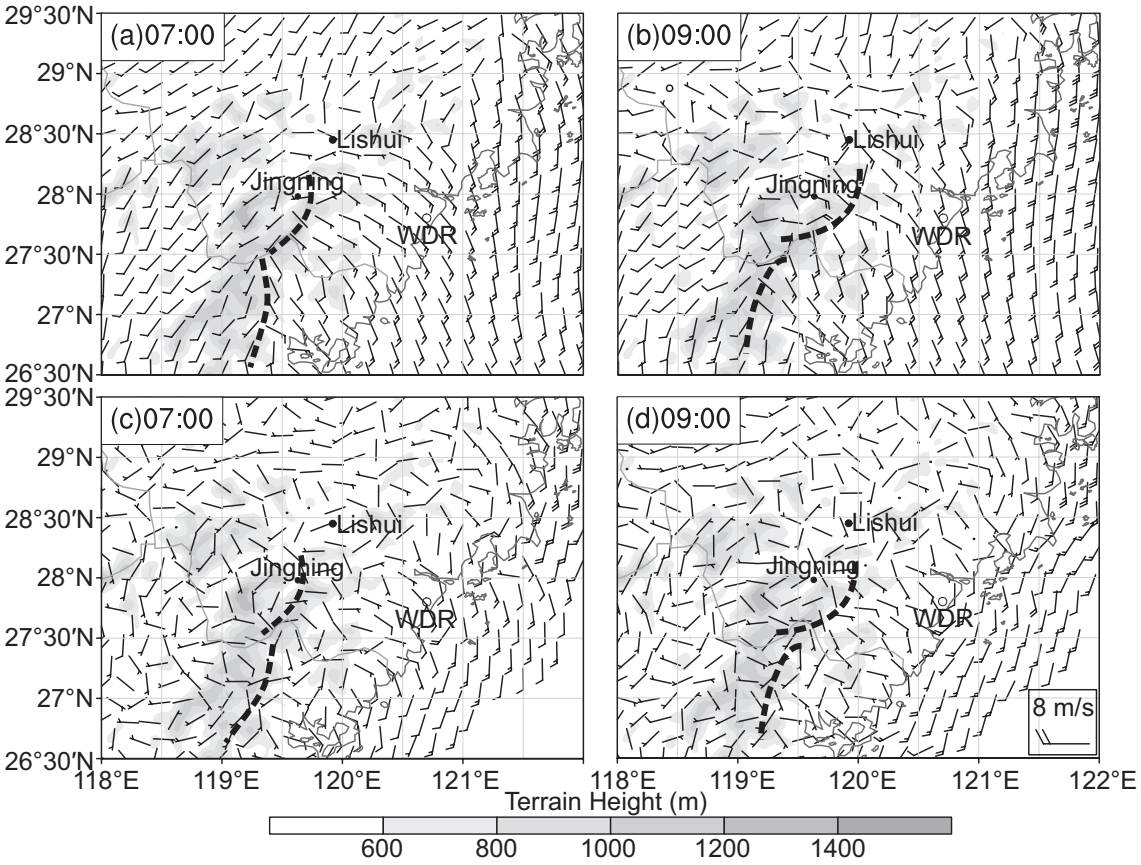

Fig. 4. Comparison between the (a, b) WRF and (c, d) observed surface winds, under conditions at 0700 UTC and 0900 UTC. The thick dashed lines represent surface convergence lines. The grayscale legend at the bottom indicates the terrain height (units: m).

5. Results and discussion

5.1. *Surface stream and divergence*

To study the mesoscale features of the convective weather that occurred in the Donggong Mountains, we obtained the WRF output data of 4 km horizontal grid resolutions to analyze the evolutions of the surface stream and radar echo. Figure 6a shows an obvious 10 m surface stream at 0630 UTC; surface convergence beyond -2×10^{-4} s^{-1} appeared over the mountains. A roughly long and narrow convergence zone appeared 30 minutes later along the Donggong Mountains, accompanied by surface wind. At that time (0700 UTC), abundant low cloud was generated near the main convective cell over the mountains in the boundary cloudiness image (not shown). The strong updrafts caused by surface mesoscale convergence played a highly important role in the formation of convection clouds (Barthlott et al., 2010). The above analysis shows that convergence centers appeared over this mountainous terrain, and the corresponding convective cells originated at the convergence centers. Figure 6b shows that radar echoes A and C occurred in the convergence zone over the mountainous terrain. From a different perspective, the cross-section of cell C (Fig. 6f) indicates that from the mountaintop upward to approximately 2 km, strong convergence was present. Above this level (2–3 km), strong divergence forced the low-level flow to lift strongly. Thus, the dynamic conditions were important in rapidly triggering the convection. The contour lines of the westerly wind component (solid black line) in Fig. 6f show that the westerly wind component mainly appeared on the west side and east side of cell C above 2 km; however, the low-level flow on the east side of cell C was a marine current from the East China Sea. These two flows met in the mountains and constituted vertical characteristics of low-level convergence and mid-level divergence. New small cells generated in the convergence zone over the peripheral mountain at 0730 UTC (Fig. 6c). At this time, cells A and C underwent further development and had smaller displacement and extension toward the northeast. However, the locations of the convergence centers that generated the convective cells over the mountains showed no change (Figs. 6c and d). At 0820 UTC, at the location of the generation of cell A, a new convective cell (B) was created by the convergence center and developed into a strong convective cell in a short time. At this time, all three convective cells (A, B and C) had matured and organically combined to form a short squall line along the southwest–northeast direction of the mountains.

5.2. *CI*

The above analysis indicates that cell C played a major role in the generation of the short mountain squall line. To

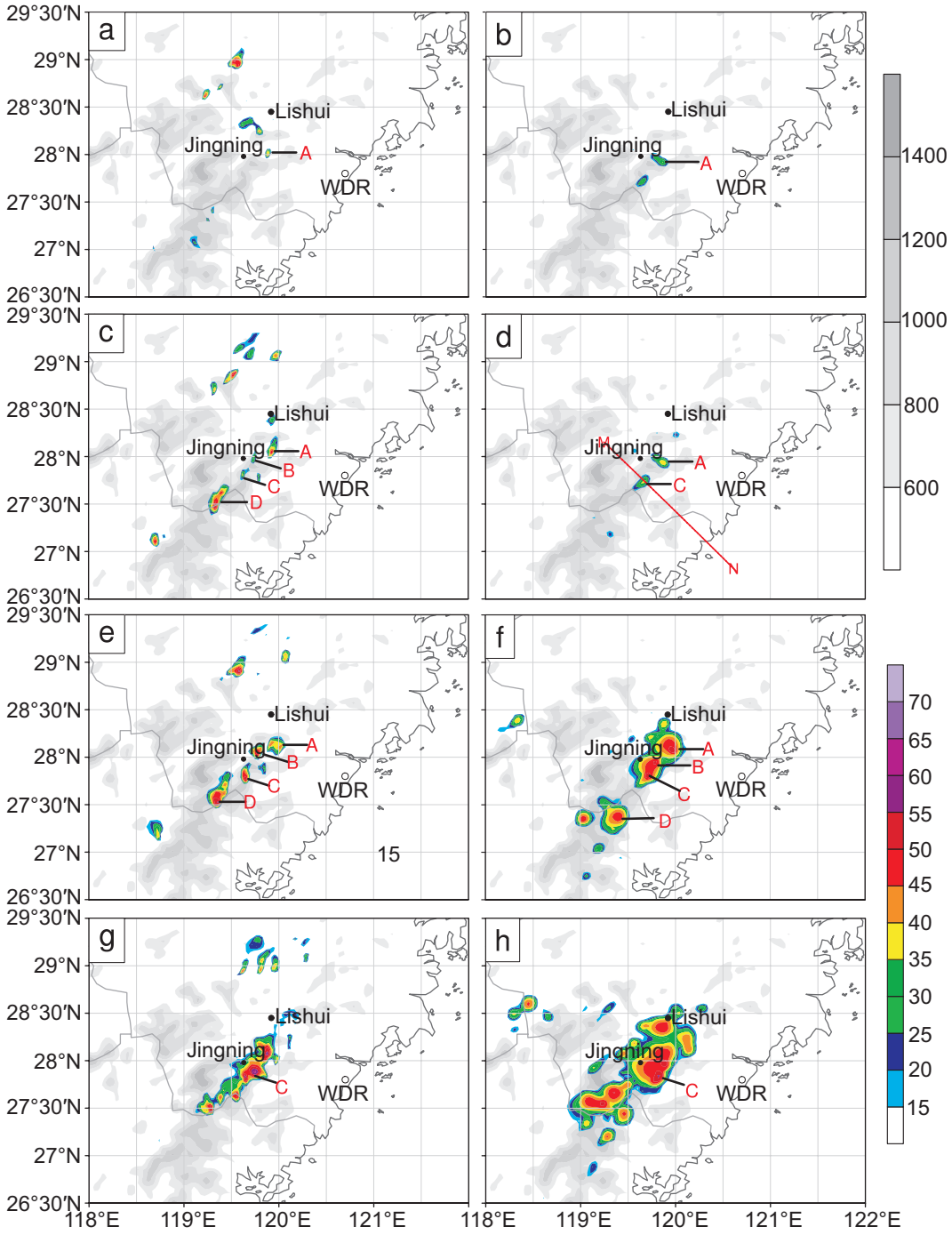

Fig. 5. Comparison of (a, c, e, g) observed and (b, d, f, h) WRF-simulated composite reflectivity. The legends of terrain height (units: m) and radar reflectivity (units: dBZ) are respectively displayed on the upper- and lower-right sides of the images. The line M–N in (d) indicates the location of the cross section shown in Fig. 7. A, B, C and D in are four echo cells listed from northeast to southwest.

realize the occurrence of orographic convection, further analysis of convective cell C was required.

Using fine mesh data, the M–N cross-section line shows meteorological factors that changed over time (Fig. 7). Figure 7 shows that the water vapor mixing ratio extended from the sea to the inland mountain area in the lower atmosphere, and the water vapor vertical gradient in the mountains was clearly low in the high-humidity area. Initially, the easterly wind from the sea surface within the boundary layer passed P_1 and P_2 and moved deep into P_3 until it met the westerly wind (Fig. 7a). With time, the east and west winds produced vertical disturbances within the boundary layer (brown line at P_2 in Fig. 7b). Consequently, water vapor mixing took place along these updrafts (Figs. 7c and d). At 0650 UTC (Fig. 7e), the disturbance flow together with the water vapor mixing ratio broke through the LCL (white thick line at

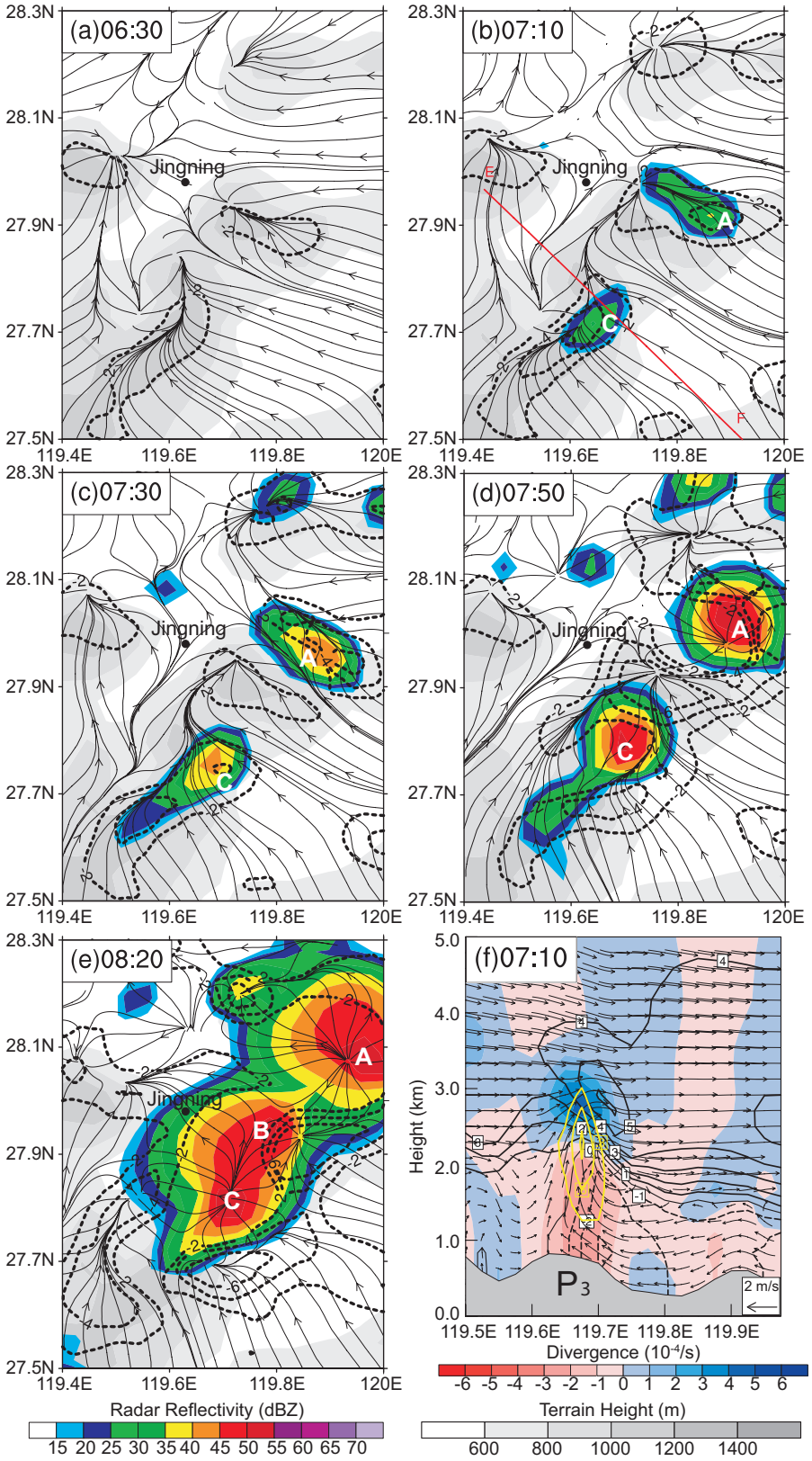

Fig. 6. (a–e) Simulated surface stream line fields, divergence fields (black dotted lines; units: 10^{-4} s^{-1}) and radar echoes; cells A, B and C are the same as the echo cells in Fig. 5e. The gray shading is the same terrain height as shown in Fig. 1b. (f) WRF-simulated cross section along line E–F of cell C shown in (b) at 0710 UTC (red line). In (f), the colored shading is the divergence (units: 10^{-4} s^{-1}). The black contours indicate the wind zonal component; the interval is 1 m s^{-1}. Yellow contours denote vertical velocity greater than 0.3 m s^{-1}.

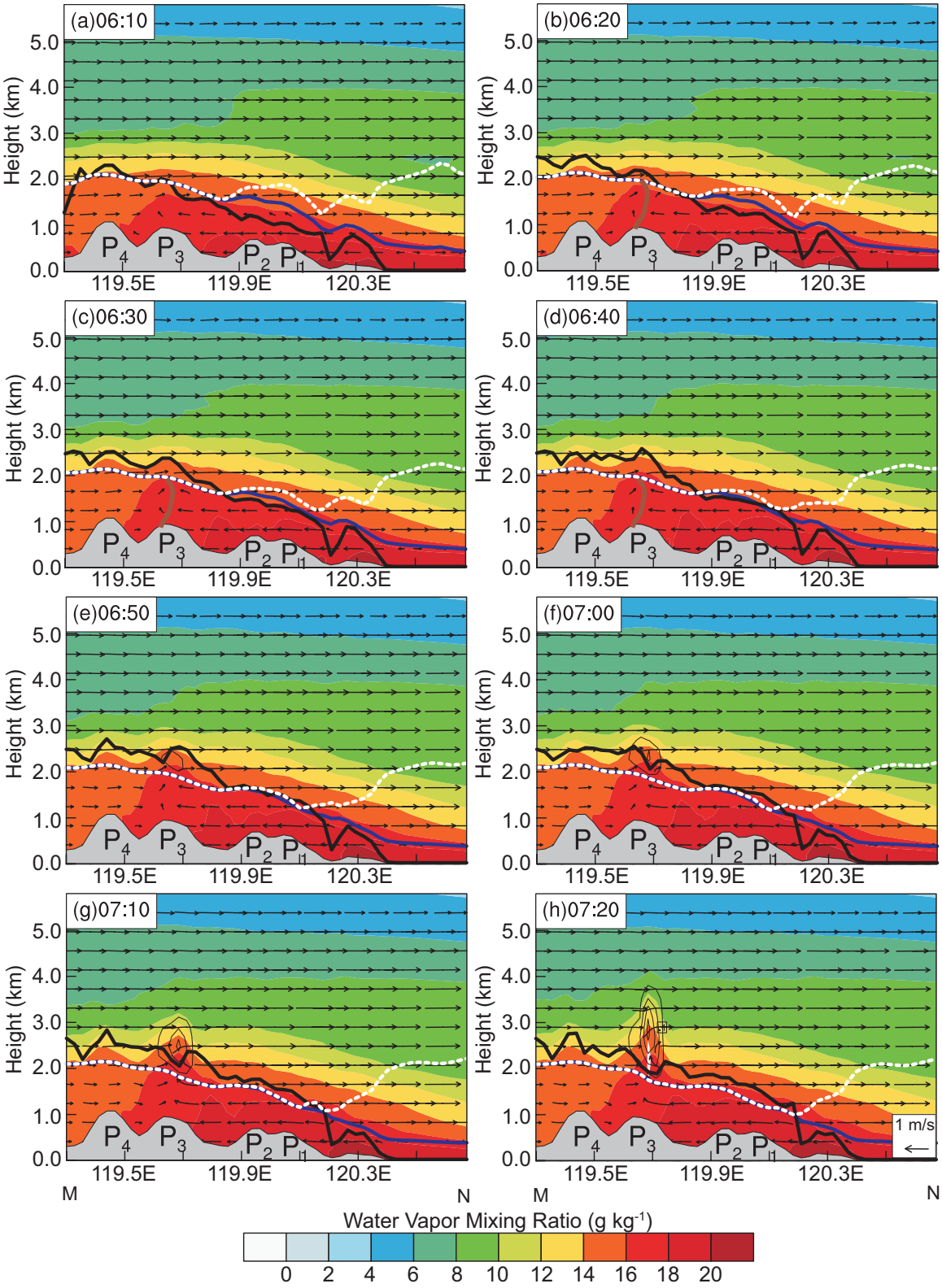

Fig. 7. WRF-simulated cross sections along line M–N of cell C shown in Fig. 5d. The background field of the water vapor mixing ratio (colored shading; units: g kg^{-1}) is shown along with horizontal wind vectors in the overlying cross section. The dark gray shading indicates four peaks in the terrain, marked P_1, P_2, P_3 and P_4. The thin black contours are the cloud water mixing ratio values (units: kg kg^{-1}; the interval is 0.3 kg kg^{-1} from 0.1 kg kg^{-1}). The thick black line denotes the PBL; the thick white dotted line is the LFC; the thick blue line is the LCL; and the brown lines in (b–d) are convergence lines at the CI location. The white shading in (h) is radar reflectivity exceeding 35 dBZ.

P_3), forming clouds above the height of approximately 2 km. Subsequently, the cloud water mixing ratio (thin black solid line in Fig. 7e) rapidly increased, moved upward vertically, and the updrafts broke through the LCL and the level of free convection (LFC) above the mountaintop completely (Figs. 7f and g). The radar echo exceeded 35 dBZ, at 0720 UTC (gray area in Fig. 7f).

The convective cells were generated at the convergence center of the surface stream over the mountains (Fig. 6b). Vertical cross sections at the same time (Fig. 6f) suggest that the convergence extended upward to 2 km , within the boundary layer, whereas the divergence existed above 2 km. The maximum speed of the zonal wind on the eastern side of cell C at 2.5 km was the main cause for the divergence above 2 km. This suggests a relatively strong southwest low-level jet above 2 km in the Donggong Mountains. The vertical coupling relation between the divergence on the upper-right side of P_3 and the convergence on the lower-right side caused the convection to develop rapidly. The low-level easterly flow was dominant over the east of mountains; however, this turned to southwesterly flow at the edge of the subtropical high in the mid-low levels, such that a low-level warm advection structure formed. The wind veer with increased height in the low level formed unstable stratification, and the warm moist flow from the southeast of the mountains was lifted upward with a vertical speed of 0.9 m s^{-1} when it met the mountains. This was shown in the slope of P_3 near the peak. Clearly, the dynamic lifting effect owing to the high mountains, together with the low-level convergence, made the updrafts reach the LCL quickly, and the condensation of water vapor formed the orographic clouds. Radar reflectivity that greater than 35dBZ was then observed because of the effect of the mountains (Fig. 7h).

The LCL and LFC, as critical indicators of atmospheric instability, were at constant altitude before the convective cells appeared (0710 UTC). Subsequently, both decreased gradually; however, at the start of convection, both decreased rapidly (0720 UTC). The decrease in the LCL was higher, and the low LCL was conducive to moisture condensation. The location of cell C was characterized by high CAPE (>2000 J kg^{-1}) and extremely low convective inhibition (CIN) (≈0.1 J kg^{-1}). The joint occurrence of low CIN and high CAPE, combined with the low LCL and LFC, increased the probability of severe convection, which is of significance to the forecasting of convection (Ziegler et al., 1997; Zhang, 2003).

5.3. *Instability mechanism*

To observe the temporal and spatial variations of the convective cell C, time–height plots of the simulated cell C (the location of cell C in Fig. 5e) are shown in Fig. 8. It can be seen that the low-level southeasterly (dashed line in Fig. 8a) from the sea gradually strengthened and moved upward with time (note: in order to make the spatiotemporal diagram and cross-section diagram look similar, we set the time coordinate from right to left to indicate that the right of the figure is the ocean and the left is the mountainous area). Before the convection triggered (0710 UTC), there was a 2 m s^{-1} zonal component near the surface. Meanwhile, the westerly wind strengthened above the boundary layer in the lower troposphere over the terrain and the meridional component exceeded 5 m s^{-1}. That is, the southeasterly airflow strengthened in the low level, the southwesterly airflow strengthened in the upper layer, and the location of CI appeared at the overlap between the two enhanced airflows. Thus, it can be seen that enhanced vertical shear over the mountains was conducive to a decrease in Richardson number to form instability, and the water vapor and temperature conditions made it easy for convection to develop. Also, the equivalent potential temperature strengthened and moved upward with time (Fig. 8a). When the low-level easterly and mid-level westerly wind reached their highest values, the equivalent potential temperature gradient also reached a maximum, as did the vertical gradient of wind speed, and clouds started to form at about 2 km at the location of the easterly turning to westerly wind (Fig. 8a). This apparent wind conversion, increased wind speed and strong equivalent potential temperature gradient favored the accumulation of convective instability energy and the formation of convective instability stratification. As shown in Fig. 6, the surface convergence provided the disturbance conditions for the convection. In contrast, as can be seen from the time–height plots of the cloud water mixing ratio and humidity (Fig. 8b), the high-humidity area almost exactly matched the large area of the equivalent potential temperature gradient; therefore, the significant humidification at approximately 2 km helped to trigger this severe convection. Interestingly, Fig. 8 shows that the humidifying layer mainly appeared at the top of the boundary layer above 1 km, as well as above the zero line of the zonal component and near the equivalent potential temperature of about 350 K, where the level of wind direction shifted and a rapid vertical decrease in equivalent potential temperature occurred. The relative humidity and cloud water mixing ratio showed no obviously upward development until the convection initiated. This illustrates that before the severe convection occurred over the mountainous terrain, relative humidity first accumulated in the overlapping area of the southeasterly and southwesterly airflow, almost near the top of the boundary layer. When the vertical gradient of equivalent potential temperature increased gradually, the wind speed reached a certain condition, and dynamic conditions such as convergence were satisfied, the convection initiated.

According to Fig. 8b, a new horizontal water vapor flux (not shown) was calculated along the boundary layer to check the source of moisture. In this layer, the water vapor flux, together with the wind, showed that moisture was continually transported into the convection region along with the southwesterly. Therefore, large amounts of water vapor were carried by the low-level southwesterly airflow, which also facilitated convection. Weckwerth (2000) and Lascaux et al. (2004) proved that, in addition to low-level convergence, water vapor at the boundary layer is critical to a convective system. Moreover, the southwesterly flow pushed the clouds and convective cells to move northeastward.

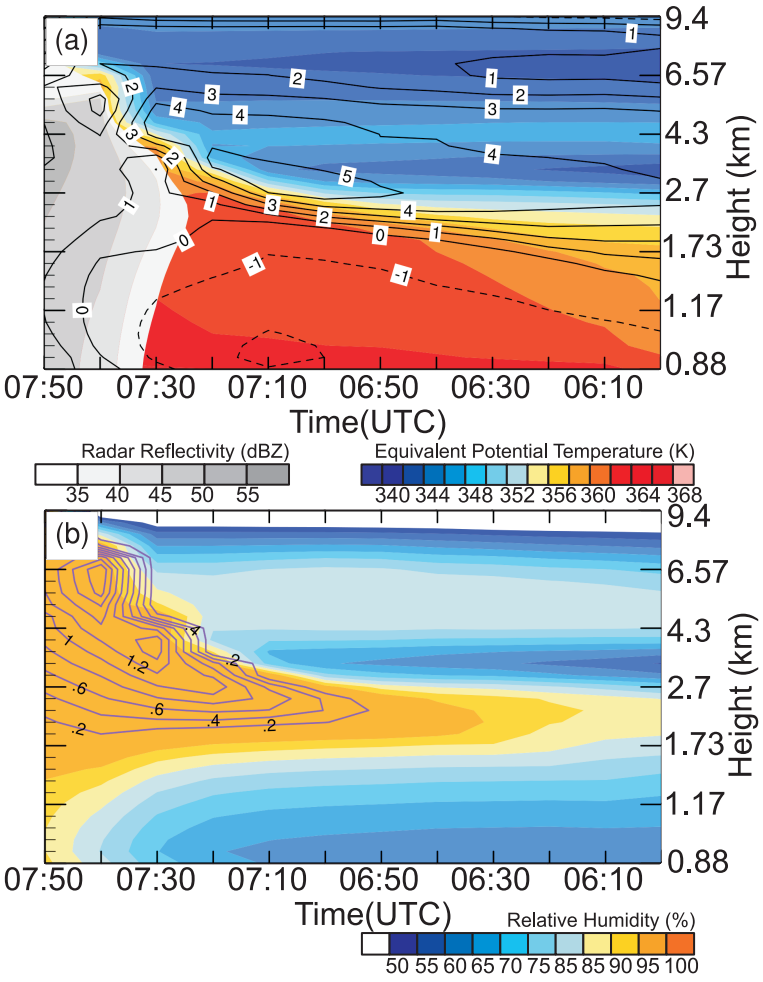

Fig. 8. (a) Time–height plot of the equivalent potential temperature (units: K), radar reflectivity (above 35 dBZ; gray shading) and zonal wind (black contours; interval: 1 m s^{-1}) in cell C (Fig. 5e). (b) Time–height plot of relative humidity (units: %) and cloud water mixing ratio (purple contours; units: g kg^{-1}) in cell C (Fig. 5e). The layer number of sigma is the left *y*-axis and the height (units: km) is the right *y*-axis. Note that the *x*-axis should be read from right to left.

6. Effect of southeasterly airflow

From Figs. 6 and 7, the convergence caused by the southeasterly wind from eastern sea and the prevailing southwesterly airflow in the Donggong Mountains was critical to the strong convection on 5 July 2012. Xu et al. (2010) studied the observed relation between the windward slope and orographic precipitation in the eastern coastal areas of China, and reported the terrain to be the most important factor affecting the proportion of windward slope rainfall in the total precipitation, and the windward slope rainfall increases during the summer monsoon because of the difference in the water vapor source and average wind speed. A Global Forecast System ($0.5° \times 0.5°$) dataset was used and a new coordinate system was created with X' and Y' axes. To study the strength of the wind from the ocean toward the land, the surface zonal and meridional wind vectors were decomposed to the X'–Y'' coordinates. Figure 9a shows the daily average wind contour at 0600 UTC in July 2012 for sigma (WRF Eta) level = 0.995. Figure 9b shows the wind contour map at 0600 UTC 5 July 2012. The positive values represent wind from the ocean toward the land, and vice-versa for the negative values. Figure 9a shows that the surface monthly average wind field comprised airflow from the sea to the land, with the average speed of wind that perpendicular to the shoreline reaching 7 m s^{-1} at 0600 UTC, and the wind speed gradually diminishing at 100 km inland. The Donggong Mountains represented the low wind speed zone, and there was a clear speed gradient between the mountains and the coastline. The lower atmosphere was affected by enhanced southeasterly airflow and the coastal mountains, which easily caused convergence on the windward slope of the mountains.

Figure 9b shows that the center of the maximum value of the southeasterly wind from the sea on 5 July was stronger than the average values in Fig. 9a. The seasonal low-level southeasterly wind increased to 10 m s^{-1} on 5 July and moved further inland. Furthermore, the wind speed on the side of the mountains far from the coastline was negative, suggest-

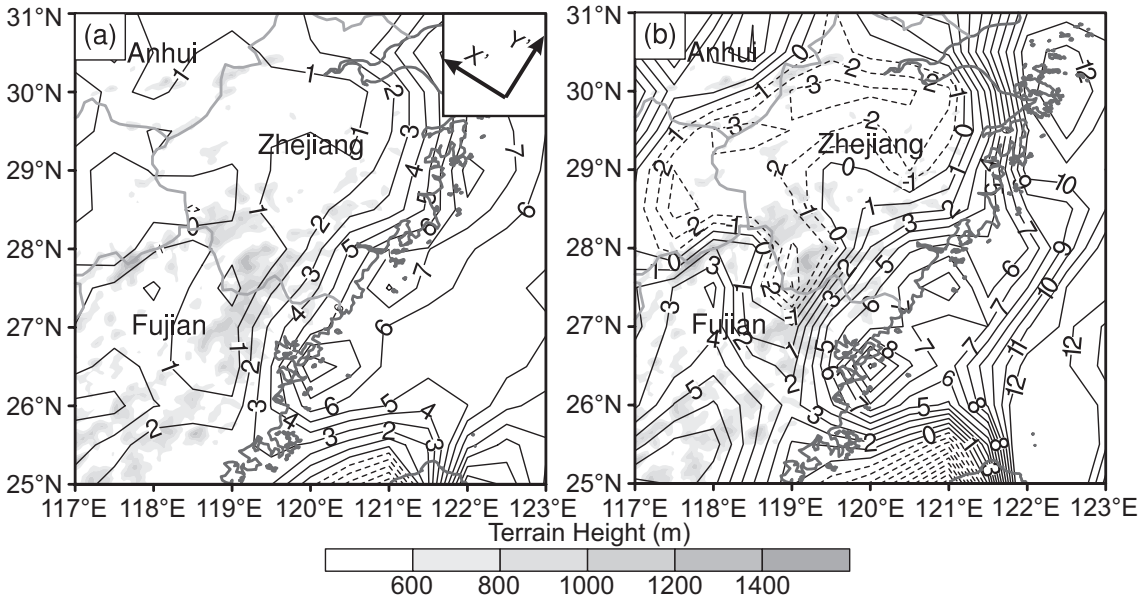

Fig. 9. (a) Average daily wind contours at 0600 UTC in July 2012 for the height of sigma = 0.995. (b) Wind contours (units: m s^{-1}) at 0600 UTC 5 July 2012. The wind contours fit into the new X' and Y' axes coordinate system [shown in the top-right corner of (a)]; X' is perpendicular to the shoreline, pointing inland, and Y' is parallel to the shoreline, pointing northeast.

ing that the wind component from the mountains to the sea increased the wind speed gradient on the windward slope of the mountains and enhanced convergence. Therefore, it is necessary for convective storms on coastal mountains to have increased winds from the ocean toward the land and decreased mountain winds from the mountains to the sea. On 5 July 2012, the two south-deflected airflows produced stronger than usual convergence and convective cells over the Donggong Mountains. The combination of water vapor conditions and topography ultimately produced the short squall line.

7. Summary and conclusions

A short squall line occurred on 5 July 2012 in the southern mountainous area of Zhejiang Province. The weather conditions produced heavy rain, gales and hail, causing significant damage to local communities. To explore the triggering conditions of the severe convection at Lishui, a numerical simulation experiment of the severe convection over the mountains was conducted using the mesoscale WRF numerical model with three nested domains. Results showed that the physical assumptions in the experiment were realistic and, thus, the simulation results satisfactory. Based on the simulation, the main conclusions of this study can be summarized as follows:

The simulation results matched the observations well. In particular, the radar echoes in the model realistically reproduced the convective cells that originally generated and then developed along the mountains, forming the squall line that moved to the northeast coast before ultimately disappearing.

There was always a convergence line over the Donggong Mountains during the severe convection. The convergence centers of the surface streamline all appeared over the mountainous terrain and triggered new convective cells. Then, the short squall line was generated along the mountains because of the movement and combination of these convective cells. Consequently, ground-level convergence was critical to the generation and development of the convective cells (mainly the CI location).

The vertical coupling relation between the convergence within the boundary layer and the divergence caused by the strong southwest low-level jet above the boundary layer was critical to the rapid development of the convection under dynamic conditions. There was always a high-humidity area from the coastline of southern Zhejiang to the Donggong Mountains, while the sea wind was affected by the orographic uplift on the windward slope. The uplifted airflow that carried the high moisture broke through the LCL and formed convective clouds above the LCL. The CI location appeared at the overlap between the enhanced zonal and meridional components, as well as in the area of high wind shear and equivalent potential temperature gradient. Furthermore, this type of configuration helped to generate convectively unstable stratification. In contrast, if the LCL at the CI location was low, the moist air was easily uplifted to the LCL, causing water vapor condensation.

The low-level southeasterly airflow from the eastern sea was critical to the severe convection in this study. The surface monthly average wind field showed obvious airflow from the sea to the land, and the average speed of wind perpendicular to the shoreline reached a maximum in the coastal sea and gradually decreased inland from the coast. The Donggong Mountains represented a zone of low wind speed; therefore, there was an obvious wind speed gradient between the moun-

tains and the coastline, and the lower atmosphere was where convergence formed on the windward slope of the mountains when affected by marine currents and the coastal mountains. Therefore, convective storms over coastal mountains require both high winds from the ocean toward the land and high mountain winds from the mountains toward the sea. When southeast and southwest winds in southern Zhejiang Province are strong during summer, the two airflows described in this study can easily produce stronger than usual convergence over the Donggong Mountains, thus creating convective cells owing to the effect of topography that, in this case, produced the short-lived squall line.

Acknowledgements. Sponsored by the National (973) Program on Key Basic Research project entitled "Observation, Prediction and Analysis of Severe Convection of China" (Grant No. 2013CB430104) and the National Natural Science Foundation of China (Grant No. 41575047).

REFERENCES

Anderson, H. A., 2010: Characteristics of decaying storms during lightning cessation at Kennedy Space Center and Cape Canaveral Air Force Station. M.S. thesis, Department of Meteorology, Florida State University, 75 pp.

Barthlott, C., and D. J. Kirshbaum, 2013: Sensitivity of deep convection to terrain forcing over Mediterranean islands. *Quart. J. Roy. Meteor. Soc.*, **139**(676), 1762–1779.

Barthlott, C., J. W. Schipper, N. Kalthoff, B. Adler, C. Kottmeier, A. Blyth, and S. Mobbs, 2010: Model representation of boundary-layer convergence triggering deep convection over complex terrain: A case study from COPS. *Atmos. Res.*, **95**(2–3), 172–185.

Byers, H. R., and R. R. Braham, 1949: *The Thunderstorm: Report of the Thunderstorm Project*. U. S. Government Printing Office, 287 pp.

Chen, F., and J. Dudhia, 2001: Coupling an advanced land surface–hydrology model with the Penn State–NCAR MM5 modeling system. Part II: Preliminary model validation. *Mon. Wea. Rev.*, **129**, 587–604.

Chen, M., B. P. Fu, and Q. Yu, 1995: Influence of topography on storm rainfall. *Acta Geographica Sinica*, **50**(3), 256–263. (in Chinese)

Hong, S. Y., and J. O. J. Lim, 2006: The WRF single-moment 6-class microphysics scheme (WSM6). *Journal of the Korean Meteorological Society*, **42**(2), 129–151.

Janjić, Z. I., 1994: The step-mountain eta coordinate model: Further developments of the convection, viscous sublayer, and turbulence closure schemes. *Mon. Wea. Rev.*, **122**(5), 927–945.

Kain, J. S., and J. M. Fritsch, 1993: Convective parameterization for mesoscale models: the Kain-Fritsch scheme. *The Representation of Cumulus Convection in Numerical Models*, K. A. Emanuel and D. J. Raymond, Eds., Amer. Meteor. Soc., 165–170.

Lascaux, F., E. Richard, C. Keil, and O. Bock, 2004: Impact of the MAP reanalysis on the numerical simulation of the MAP-IOP2a convective system. *Meteor. Z.*, **13**(1), 49–54.

Li, Y. Y., W. Huang, and Zhao, J. Z., 2007: Roles of mesoscale terrain and latent heat release in typhoon precipitation: A numerical case study. *Adv. Atmos. Sci.*, **24**(1), 35–43, doi: 10.1007/s00376-007-0035-8.

May, P. T., and A. Ballinger, 2007: The statistical characteristics of convective cells in a mnsoon regime (Darwin, Northern Australia). *Mon. Wea. Rev.*, **135**(1), 82–92.

Mecikalski, J. R., K. M. Bedka, S. J. Paech, and L. A. Litten, 2008: A statistical evaluation of GOES cloud-top properties for nowcasting convective initiation. *Mon. Wea. Rev.*, **136**(12), 4899–4914.

Meißner, C., N. Kalthoff, M. Kunz, and G. Adrian, 2007: Initiation of shallow convection in the Black Forest mountains. *Atmos. Res.*, **86**(1), 42–60.

Purdom, J. F. W., and K. Marcus, 1982: Thunderstorm trigger mechanisms over the southeast U. S. Preprints, *12th Conf. on Severe Local Storms*, San Antonio, TX, Amer. Meteor. Soc., 487–488.

Raymond, D., and M. Wilkening, 1980: Mountain-induced convection under fair weather conditions. *J. Atmos. Sci.*, **37**(12), 2693–2706.

Roe, G. H., 2005: Orographic precipitation. *Annual Review of Earth and Planetary Sciences*, **33**, 645–671.

Rudari, R., D. Enteldaabi, and G. Roth, 2004: Terrain and multiple-scale interactions as factors in generating extreme precipitation events. *J. Hydrometeor.*, **5**(3), 390–404.

Smith, R. B., 1979: The influence of mountains on the atmosphere. *Advances in Geophysics*, **21**, 87–230.

Tao, S. Y., 1980: *Heavy Rainfalls in China*. Science Press, 225pp. (in Chinese)

Toth, J. J., and R. H. Johnson, 1985: Summer surface flow characteristics over Northeast Colorado. *Mon. Wea. Rev.*, **113**(9), 1458–1469.

Weckwerth, T. M., 2000: The effect of small-scale moisture variability on thunderstorm initiation. *Mon. Wea. Rev.*, **128**(12), 4017–4030.

Weckwerth, T. M., L. J. Bennett, L. J. Miller, J. Van Baelen, P. Di Girolamo, A. M. Blyth, and T. J. Hertneky, 2014: An observational and modeling study of the processes leading to deep, moist convection in complex terrain. *Mon. Wea. Rev.*, **142**(8), 2687–2708.

Wilson, J. W., and W. E. Schreiber, 1986: Initiation of convective storms at radar-observed boundary-layer convergence lines. *Mon. Wea. Rev.*, **114**(12), 2516–1536.

Xu, X., Q. W. Wang, and Y. Wang, 2010: On the contribution of upslope precipitation to the observational precipitation over southeastern China. *Journal of Nanjing University (Natural Sciences)*, **46**(6), 625–630. (in Chinese)

Yue, C. J., S. T. Gao, L. Liu, and X. F. Li, 2005: A diagnostic study of the asymmetric distribution of rainfall during the landfall of typhoon Haitang (2005). *Adv. Atmos. Sci.*, **32**(10), 1419–1430, doi: 10.1007/s00376-015-4246-0.

Zhang, G. J., 2003: Roles of tropospheric and boundary layer forcing in the diurnal cycle of convection in the U. S. southern great plains. *Geophys. Res. Lett.*, **30**(24), 2281.

Ziegler, C. L., T. J. Lee, and R. A. Pielke, 1997: Convective initiation at the dryline: A modeling study. *Mon. Wea. Rev.*, **125**(6), 1001–1026.